Journal of Power Sources 285 (2015) 247–259

Contents lists available at ScienceDirect

Journal of Power Sources

journal homepage: www.elsevier.com/locate/jpowsour

Experimental modal analysis of lithium-ion pouch cells

James Michael Hooper, James Marco*

WMG, University of Warwick, Coventry CV4 7AL, UK

HIGHLIGHTS

- Experimental assessment of the frequency response of a Li-ion pouch cell.
- Assessment of the mode shapes for a Li-ion pouch cell using impulse excitation.
- Quantifying cell stiffness as a function of state of charge.
- Quantifying cell damping as a function of state of charge.
- Correlation of the cell's frequency response with road-induced vibration profiles.

ARTICLE INFO

Article history:
Received 11 December 2014
Received in revised form
12 February 2015
Accepted 15 March 2015
Available online 17 March 2015

Keywords:
Modal analysis
Vehicle vibration
Electric vehicle (EV)
Hybrid electric vehicle (HEV)
Battery testing
Noise vibration and harshness (NVH)

ABSTRACT

If future electric and hybrid electric vehicle batteries are to be designed such that the impact of vibration induced resonance is minimized, engineers tasked with the design of the vehicle's energy storage system must have a rigorous understanding of key system attributes such as the natural frequencies of the cell, the level of damping present and the mode shapes induced within the battery under mechanical load. This paper describes the underpinning theory and experimental method employed when using the impulse excitation technique to quantify the natural frequencies and mode shapes of a commercially available 25 Ah Nickel Manganese Cobalt Oxide (NMC) Laminate Pouch Cell. Experimental results are presented for fifteen cells at five different values of state of charge (SOC). The results indicate that irrespective of the energy content within the cell, the same four modes of vibration (torsion and bending) exist within a frequency range of 191 Hz–360 Hz. This is above the frequency range (0–150 Hz) typically associated with road-induced vibration. The results also indicate that the cell's natural frequencies of vibration and damping do not vary with changing values of SOC.

1. Introduction

Within the automotive and road transport sector, one of the main drivers for technological development and innovation is the need to reduce the vehicle's fuel consumption and the emissions of carbon dioxide (CO_2). Legislative requirements are motivating vehicle manufacturers and subsystem suppliers to develop new and innovative electric vehicle (EV) and hybrid electric vehicle (HEV) concepts. Within this field, a key enabling technology is the design and integration of the high voltage (HV) battery system.

The impact of mechanical vibration on the vehicle's electrical and electronic components and subsystems is known to be a major cause of in-market durability failure [1]. If excessive warranty claims are to be avoided, it is important that engineers tasked with the design of the HV battery system, properly understand the magnitude and frequency of the vibration inputs that the energy storage system will be exposed too during the vehicle's predicted life. If future vehicle battery systems are to be designed such that the impact of vibration induced resonance is minimized, engineers must have a rigorous understanding of key system attributes such as the natural frequencies of the cell, the level of damping for each natural frequency and the mode shapes induced within the cell when it is under mechanical load (e.g. the presence of bending, torsional or panting modes).

Experimental modal analysis measures the natural vibration response of a system. To ensure vehicle durability it is necessary to determine, at the design stage, the natural vibration characteristics of components, both in isolation and when they are aggregated into larger vehicle sub-systems. Recent studies [2] have highlighted that if a system was allowed to vibrate at one of its modal frequencies

* Corresponding author.
E-mail addresses: j.m.hooper@warwick.ac.uk (J.M. Hooper), james.marco@warwick.ac.uk (J. Marco).

http://dx.doi.org/10.1016/j.jpowsour.2015.03.098

Nomenclature

Terms and abbreviations

BMS	battery management system
dB	decibels
EMS	electromagnetic shaker
EV	electric vehicle
FRF	frequency response function
HEV	hybrid electric vehicle
HV	high voltage
Li-ion	lithium ion
NMC	nickel manganese cobalt
NVH	noise vibration and harshness
PSD	power spectral density
SISO	single input single output
SOC	state of charge

Mathematical notation – symbols and units

f_{max}	maximum frequency Hz
k_p	tip stiffness Nm^{-1}
k_c	cell stiffness Nm^{-1}
m_H	hammer mass kg
m_c	cell mass kg
Q	quality-factor -
T	time s
ω	frequency $rads^{-1}$
ω_n	natural frequency $rads^{-1}$
ς	damping ratio -
$G_{xy}(f)$	cross-spectral density
$G_{xx}(f)$	auto-spectral density (x)
$G_{yy}(f)$	auto-spectral density (y)
$x(t)$	system input (time domain)
$y(t)$	system output (time domain)
$X(s)$	system input (laplace domain)
$Y(s)$	system output (laplace domain)
$H(s)$	system transfer function (laplace domain)
$H(j\omega)$	system transfer function (frequency domain)

with excessive, sustained, oscillatory motion permanent deformation or structural damage may occur. One example of an automotive component that failed through sustained excitation at one of its natural frequencies is presented within [1]. The research discusses the complete mechanical failure of the component after only 7000 km of driving [1]. The failure mode was identified using modal analysis techniques. The study found that the first natural frequency of the component occurred at 52.2 Hz and the road-load profile induced an accelerated fatigue condition within the device. Modal analysis is not limited to small components or systems. The methodology is also widely employed within the civil engineering domain, for example when assessing the structural integrity of bridges [3]. A recent study from the UK [3] highlights the application of modal analysis for understanding the undesirable swaying motion experienced when the Millennium Bridge was opened in London during the year 2000. It was identified that the 1st and 2nd natural modes of vibration for the bridge occurred between 0.5 and 1 Hz respectively and pedestrians excited these modes when they traversed the bridge [3]. Due to excessive motion of the structure and the subsequent fears for public safety, the bridge was closed until 2002, while engineer's integrated additional dampers within the bridge to reduce the amplification associated with the natural frequencies.

This paper describes the underpinning theory and experimental method employed when using the impulse excitation technique to quantify the natural frequencies and mode shapes of a commercially available 25 Ah Nickel Manganese Cobalt Oxide (NMC) Laminate Pouch Cell. From the experimental results obtained, values for cell damping and stiffness are estimated. Through the evaluation of different cells at the same SOC and at different values of state of charge (SOC), this research has been able to quantify the variability in the mechanical frequency response of the cells due to cell-to-cell manufacturing variations and stored energy.

This paper is structured as follows; Section 2 discusses the concept of mechanical testing for Li-ion cells and Section 3 introduces the experimental theory that underpins modal analysis. Section 4 describes the experimental set-up and method employed when undertaking modal analysis with a Li-ion pouch cell. Key results and discussions are presented in Section 5, with conclusions and further work presented in Sections 6 and 7 respectively.

2. Related research

Research undertaken into the mechanical testing and characterization of Li-ion cells, particularly within the context of designing and testing the vehicle's HV battery system can broadly be classified as being based on either static or dynamic test methods [2]. Irrespective of the exact methodology employed, the primary motivation for performing such experiments is often the generation of data to either parameterize or validate high fidelity finite element models of the battery system to better understand the impact of mechanical loading [2]. Research that aims to quantify pertinent material properties under a combination of different environmental conditions with varying mechanical and electrical loads includes, but is not constrained too: assessments of mechanical stress and strain within the numerous different components that comprise the cell (outer casing, electrodes, separators and current collector) [2,4–6], quantifying the creep within a representative sample of conductive material at different temperatures [6] and measuring the volume expansion of a pouch-cell during charge–discharge conditions [8].

In addition to the performance evaluation of different cell chemistries and formats, there is also a significant body of research that attempts to quantify the mechanical robustness (crashworthiness) of the cell or complete battery system. Examples of recent publications include the mechanical crushing of the cell [4,7,9], the effect of cell penetration [2,10], assessing the durability of the cell against impact [4,9] and mechanical shock [4] and understanding the fatigue conditions and possible failure modes of the battery system due to extreme variations in temperature and pressure [11,12]. The need to conduct such tests is often driven by the requirement to satisfy whole vehicle crash homologation Standards [13,14] and legislation, such as UN38.3, that governs the transportation of dangerous goods [15–17].

In recent years, there has been comparatively less research addressing the mechanical durability and vibration response of individual cells or the complete battery system. Research has been published [18] that correlates mechanical fatigue within the cell to the use of repetitive deep-discharge cycles. However, as discussed within Section 1, another of source of mechanical fatigue within the battery may well be the vibration-induced resonance resulting

from the road-profile when the battery is mounted to the sprung mass of the EV or HEV [19–21].

Only a single study has been identified that attempts to quantify the natural frequencies of a Li-ion pouch cell [2]. A program of experimental modal analysis is described within [2] in which impulse excitation tests are performed on a *used but serviceable* 10 Ah Li-ion pouch cell. This study observed three modes within the 0–1000 Hz range, with the first mode occurring at approximately 267 Hz. While this study validates the fundamental concept of frequency analysis of a Li-ion cell using the impulse excitation method, there are a number of shortcomings associated with the scope of the research that limit its applicability and the conclusions that can be drawn. Firstly, the study failed to quantify either the damping or the stiffness present within the cell. Secondly, only a very limited sample size of four cells was employed, with each cell maintained at the same environmental conditions and the same SOC. The aim of this research is to extend that presented within [2].

3. Experimental theory

The aim of this section is to describe the theory associated with modal analysis using impulse excitation. Particular consideration is given to the method employed to secure and mount the pouch cell during testing, the excitation technique and the interpretation of the results obtained.

3.1. Cell mounting and support

When conducting experimental modal analysis, it is necessary to ensure that the correct method of support is selected. There are typically two options available, either unrestrained (*free − free*) or clamped (*grounded*). This discussion will primarily address the unrestrained support, since this was the method employed within the experimental activity. The use of an unrestrained support medium is preferred since the results obtained reflect only the mechanical properties of the component. Rigidly clamping the component to the test fixture is only used to emulate the in-service mounting conditions of the device and therefore includes the dynamics of the component and its support structure. A further detailed discussion of each support method is provided in Ref. [22].

The definition of an unrestrained support is a where the component is freely suspended in space [22,23]. Within this ideal, the component exhibits six rigid body modes; three displacements (in the x, y, z co-ordinate axis) and three rotations around each of the three axes [22,23]. Because this ideal condition assumes that no boundary condition exists, reactions between the support and the component have a natural frequency equal to zero. In practice, components are suspended on soft springs or foam pads. As a result, a true *free–free* support condition can never be realized. The use of low-density foam pads results in the six ridged body modes occurring at very low natural frequencies. In practice a support method and component is regarded as being within the *free–free condition* if the highest natural frequency of the support medium is less than 10% of the value of the lowest natural frequency of the component under test or if there is at least a 100 Hz separation between them. The experimental results presented in Section 5, highlight a frequency separation of approximately 150 Hz between the foam pads employed to support the Li-ion pouch cells and the first natural frequency of the cell itself (irrespective of the cell's SOC).

3.2. Cell excitation and response measurement

There are three methods of excitation commonly employed when measuring the modal response of a component or system; impulse excitation (often referred to as either hammer surveying, impact testing or impact excitation), dynamic excitation and operational excitation.

Operational excitation requires the system to be subject to the actual loading profile that it will experience within the real world. This method is typically only employed when the system will be subject to a predefined loading or in conjunction with the impulse or dynamic excitation as a final verification test. Given the diverse nature of the different terrain profiles experienced by vehicles within either urban or highway environments in different parts of the world, the use operational excitation would not be appropriate to assess the natural frequency of an EV or HEV battery system. Dynamic excitation is often employed for components that may be damaged through impulse excitation [22]. Dynamic excitation typically employs a small electro-magnetic shaker (EMS) or hydraulic shaker to apply a known input (force and frequency) to the device or structure. The advantages of dynamic excitation are often cited to include a more repeatable test profile [22–24], with the ability to apply a broader range of test signals (force and frequency range). However, the resources required to implement a test program are equally more demanding. The financial cost of the EM or hydraulic shaker may well be prohibitive for a number of end-users [22,24]. Similarly, the effort required to emulate the desired *free–free* test condition will require the design of a bespoke test assembly in which the cell is suspended onto the shaker. For these reasons, impulse excitation was defined as the desirable test method. For completeness, further information on both operational and dynamic excitations methods can be found in Refs. [22,25].

In addition to those reasons highlighted above, the reasons often cited for the use of impulse excitation include; reduced test preparation time, no specific requirements for test infrastructure (particularly when employed to undertake unrestrained testing) and the cost of the test equipment is not prohibitive [22–25]. Impulse excitation is performed using an impact device such as an instrumented hammer of calibrated mass. A typical instrument is

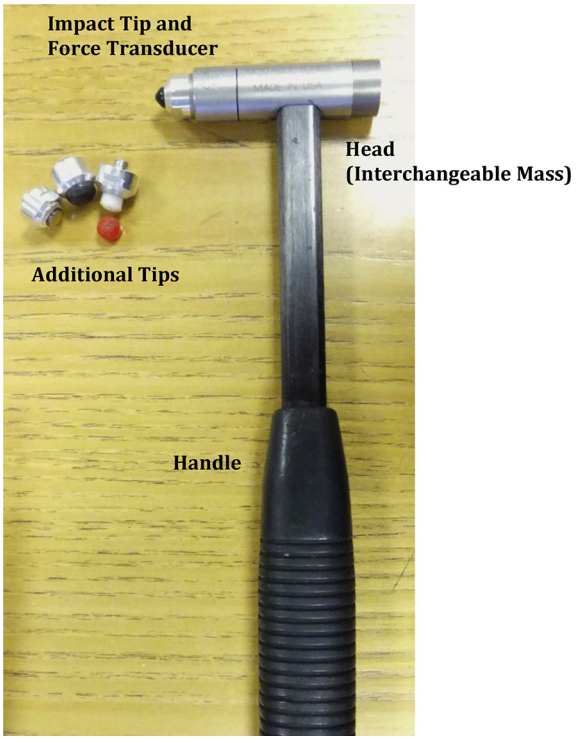

Fig. 1. Example instrumented impact hammer for impulse excitation.

shown in Fig. 1. The device consists of a head which can allow for the inclusion of additional masses, a calibrated force transducer, an interchangeable impact tip and handle [22,24]. A collection of tips are often supplied, each of different stiffness to allow the user to vary the characteristics of the impulse applied. The force transducer detects the magnitude of the impact force that is assumed to be equal and opposite to that experienced by the structure. As discussed within [22,25], through careful selection of the hammer mass (H_m) tip stiffness (k_p), the upper frequency (f_{max}) that the input excitation will excite can be approximated using (1).

$$f_{max} = \frac{1}{2\pi}\sqrt{\left(\frac{k_p}{H_m}\right)} \tag{1}$$

The frequency (f_{max}) defines the cut-off frequency above which the energy supplied by the hammer reduces at a rate of 40 dB per decade. Section 4 discusses further the actual instrumentation employed within the experimental work, including the selection of hammer mass and tip stiffness to evaluate the frequency response of the NMC Li-ion pouch cell.

Publications [22,24,25] state that the disadvantages associated with the use of impulse excitation include: the limited control of the experimental frequency range and a relatively high potential for operator error and measurement inaccuracy. Section 4 discusses further the steps employed to post-process the experimental results to reduce potential inaccuracy through *spectrum averaging*.

3.3. Mounting of accelerometers

A key requirement for any modal analysis is the accurate measurement of the applied force and the response of the component. For impulse excitation, the input force is measured via a load cell installed within the impact hammer. Conversely, the vibration response of the component is measured using either single or multiple accelerometers mounted to the surface of the component. When mounting the accelerometers, the combined weight of the sensor including any mounting interface or adhesive must be less than 1% of the mass of the component [22]. As discussed within [22], above this threshold there is the potential to significantly change the natural frequency of the component and its frequency response. When selecting an accelerometer, there is typically a comprise between component weight and sensitivity; reducing the mass of the sensor will reduce its sensitivity, but will increase the frequency range of measurement [22].

There are multiple methods of bonding the accelerometers to the component. These include stud mounting, magnetic mounting or pad mounting. For the experimentation discussed in Sections 4 and 5, an adhesive was employed to bond the accelerometer to the surface of the cell. Compliant materials, such as mounting waxes or interface mounts, can create a mechanical filtering effect by isolating and damping high-frequency transmissibility [26]. As discussed within [27], Petro-wax is often employed as it requires minimal surface preparation and does not significantly reduce the effective frequency range of the transducer [27]. Petro-wax is known to be a durable adhesive at lower temperatures, has a quick application time and no cure time. However, its transmissibility properties at high levels of force are limited and as such, it is only suitable for frequencies below 10 kHz [26]. It is also significantly affected by temperature elevation above a threshold of 30 °C.

3.4. Signal analysis and interpretation

3.4.1. System dynamics

Impulse excitation is based on the assumption that the component under evaluation is a Linear Time Invariant (LTI) system. *Linearity* means that the relationship between the input and the output of the system follows the law of *superposition*. Namely, if $x_1(t)$ produces a response $y_1(t)$ and $x_2(t)$ produces a response $y_2(t)$, then a scaled and summed input of $ax_1(t) + bx_2(t)$ will produce an output: $ay_1(t) + by_2(t)$. *Time invariance* means that for the input $x_1(t)$ the output is $y_1(t)$, the input $x_1(t - T)$ will produce the same output delayed in time by a value of T: $y_1(t - T)$.

The Impulse function, $\delta(t)$, is defined as a signal in which the amplitude (A): $A \rightarrow \infty$, while the time duration of the signal (t): $t \rightarrow 0$. The value (area) of $\delta(t)$ is unity. For an LTI system:

$$Y(s) = H(s)X(s) \tag{2}$$

where $Y(s)$ is the output, $X(s)$ is the input and $H(s)$ is the transfer function that defines the dynamics of the system and s is the Laplace operator. When $X(s)$ equals unity, the output $Y(s) = H(s)$. Given that:

$$H(j\omega) = H(s)_{s=j\omega} \tag{3}$$

means that the resulting frequency response function (FRF) characterises completely the dynamics of the system in terms of both gain and phase:

$$Gain = |H(j\omega)| \tag{4}$$

$$Phase = \angle H(j\omega) \tag{5}$$

When quantifying the damping ratio and stiffness of the cell, the assumption is made that the system is dominated by second-order dynamics. As a result, the system transfer function can be approximated by:

$$H(j\omega) = \frac{\omega_n^2}{(\omega_n^2 - \omega^2) - j2\varsigma\omega_n\omega} \tag{6}$$

where ω_n defines the natural frequency and ς the damping ratio. Assuming the cell can be represented by a 2nd order mechanical (mass-spring-damper) system and with reference to (6), the bulk stiffness within the cell can be approximated from:

$$k_c = \omega_n^2 m_c \tag{7}$$

where k_c and m_c define the cell stiffness and mass respectively. From the FRF measured, the level of damping for each natural frequency observed can be approximated from:

$$\varsigma = \frac{1}{2Q} \tag{8}$$

where Q is defined as the Quality-Factor and equal to:

$$Q = \frac{\omega_n}{\Delta\omega} \tag{9}$$

where $\Delta\omega$ defines the width of the range of frequencies for which the energy within the system output is at least half of its peak value.

3.4.2. Coherence

The coherence function, $G_{xy}(f)$, given by (10), indicates the portion of the output energy correlated to the input energy [22].

$$G_{xy}(f) = \frac{|G_{xy}(f)|^2}{G_{xx}(f)G_{yy}(f)} \tag{10}$$

where $G_{xy}(f)$ defines the cross-spectral density between the input x

and the output y, and $G_{xx}(f)$ and $G_{yy}(f)$ define the auto-spectral density of the signals x and y respectively. $G_{xy}(f)$ is used in experimental modal analysis to identify excess noise or uncertainty between the input and the output [22,28,29]. Equation (10) yields a value between zero and unity. A value of one at a given frequency indicates that all of the response energy is due to the stimulus or input signal. Conversely, a value of zero indicates that there is no correlation between the input and output signals [22]. When reviewing results, a value of $G_{xy}(f)$ greater than 0.9 is deemed to represent a valid measurement point.

3.4.3. Mode shape definition

To identify the mode shapes generated within a given structure multiple FRFs must be recorded from multiple locations and a response matrix generated in which each FRF is mapped to a location and excitation. Mode shapes cannot be determined from a single FRF and/or from a single test position. Fig. 2 presents an illustrative example that explains the source of the mode shapes [25,30].

Within this example there are six locations on a rectangular structure where the input excitation is applied. Fig. 2(a) shows that the first mode shape for the structure, correlating to the first natural frequency, is a bending moment. The bending moment is produced since the FRF at positions 1, 2, 5 and 6 are in anti-resonance, while the response in positions in 3 and 4 are in resonance. Correlating the FRFs to a simple mesh model of the structure facilitates the definition of the mode shape. Similarly, Fig. 2(b) shows the mode shape for the second natural frequency, in which the FRF at positions 1 and 6 are positive whereas at positions 2 and 5 they are in anti-resonance. As a consequence, the mode shape corresponding to the second natural frequency is torsion. The experimental method and results presented in Sections 4 and 5 describe the use of MATLAB and IDEAS to generate the respective FRFs and mode shapes for the Li-ion cells.

4. Experimental setup

4.1. Cell conditioning

The frequency response of fifteen commercially available 25 Ah pouch cells was evaluated. In order to study the impact of cell-to-cell variations and the differences in the cell's FRF that may arise due to changes in SOC, three cells were charged to the SOC values: 10%, 25%, 50%, 75% and 90%. Table 1 defines the SOC value for each of the fifteen cells under test. The SOC range was primary selected, since as reported within [1,2] to militate against the effects of cell degradation the battery management system (BMS) will often seek to constrain the SOC and limit excursions to values greater than 90% or less than 10%. Furthermore, while the theory of modal analysis could be applied to a damaged cell, all of the cells employed within this study were deemed to be within the manufacturer's specification. Overcoming the health and safety implications of testing a damaged cell was deemed to be outside of the scope of this study. In addition, even when performing such experimental research it would be desirable to have the FRF for an undamaged cell to facilitate a comparison between the two datasets (for example to identify any changes in the natural frequency, phase-shift, stiffness or damping within the battery).

Table 1
Preconditioned cell SOC values for the experimental modal analysis.

SOC (%)	Cell quantity	Cell serial numbers prepared to this SOC
10	3	259, 267 and 268
25	3	260, 261 and 266
50	3	262, 264 and 265
75	3	263, 269 and 270
90	3	273, 275 and 276
Total	*15*	

The constant current (CC) constant voltage (CV) charging/discharging procedure employed to pre-condition the cells is summarized below:

- Cell discharged at 1C (CC-CV) to manufacturer's defined lower voltage threshold at which point the cell voltage was allowed to stabilize for 3 h.
- Cell charged at 1 C (CC-CV) to manufacturer's defined upper voltage threshold at which point the cell voltage was allowed to stabilize for 3 h.
- Cell discharged at 1 C (CC-CV) to a voltage threshold commensurate with the target SOC value and allowed to stabilize for 3 h.

During the pre-conditioning phase, the storage and cycling of each cell was undertaken within a temperature-regulated environment (T = 25 °C).

4.2. Modal analysis

As discussed in Section 3, the method of experimental modal analysis chosen was to conduct a *hammer survey* via a Single Input Single Output (SISO) method. Fig. 3 displays the grid layout marked onto each cell. Each intersection (locations 1–25) defines a unique impact point. Each cell location was impacted five times and the results of each measurement averaged to generate a SISO response for that test location.

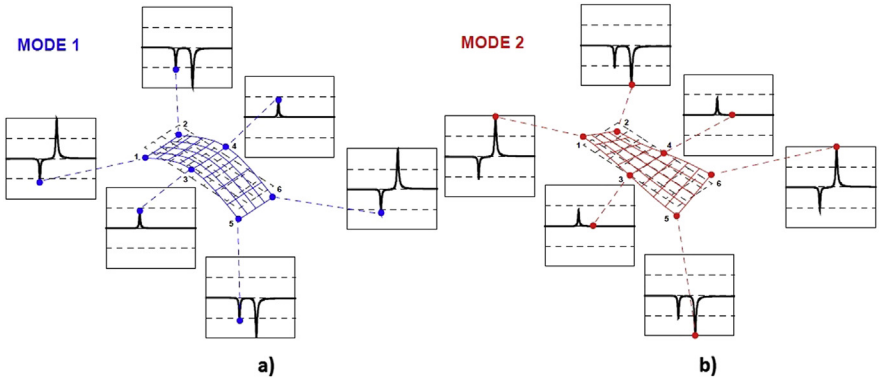

Fig. 2. Definition of mode shapes from multiple frequency response functions [30].

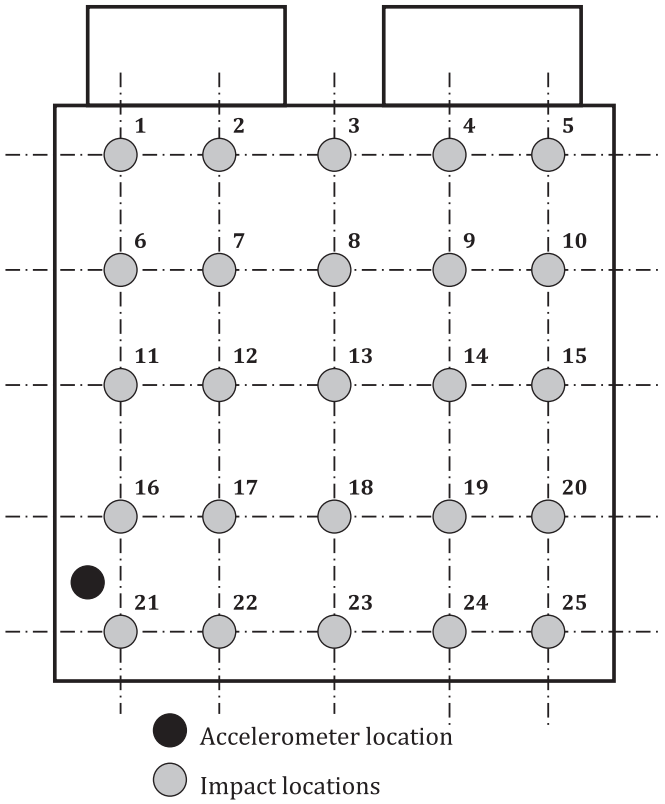

Fig. 3. Grid layout employed for SISO impulse excitation tests.

The testing of each cell was conducted within an air-conditioned laboratory, with a regulated temperature of 21 °C. Testing was conducted using an impulse hammer (type: PCB 086C08). The mass of the hammer was 0.32 kg and the tip stiffness was approximately equal to 3158 k Nm^{-1}. From Equation (1), this provided a measurement frequency range of approximately 0–500 Hz and encompasses the region of typical road induced vibration [19]. A single axis accelerometer (type: PCB 352C65) was employed to measure the output vibration from each cell. Fig. 3 shows the location on the cell where the accelerometer was bonded. The weight of the accelerometer was 2 g (less than 0.4% of total cell mass); minimizing the possibility of experimental error through increasing the mass of the cell. Due to the irregular surface of the cell and the desire not to change the structure or to damage the cell (that may result through the use of permanent adhesives), the accelerometer was bonded to the cell surface using petro-wax. The data logger and frequency analyzer employed was a Brüel and Kjær 7539A Controller and a Brüel and Kjær 3038 type Input Module. During the modal analysis, each cell was placed on four blocks of polyurethane foam that were approximately 40 mm × 40 mm by 20 mm deep. The blocks were positioned under the four corners of the cell. Fig. 4 shows an example frequency response (magnitude plot) for one pouch cell mounted on the foam pads. It can be seen that lowest natural frequency of the cell is approximately 200 Hz, whereas the highest resonance of the foam pad occurs at approximately 36.5 Hz. As discussed in Section 3.1, this level of frequency separation between the mounting medium and the cell, confirms the required *free–free* test condition.

4.3. Data analysis and post-processing

For each cell defined in Table 1, the following method was employed to post-process the measured data and to quantify the cell's frequency response function (FRF). From Equations (4) and (5), it is possible to calculate the FRF for each of the cell's 25 impact locations. Given the geometry of each cell and the dimensions of the measurement grid shown in Fig. 3, the Brüel and Kjær software (that include elements of IDEAS functionality) is able to quantify the mode shapes for each natural frequency within the cell. The mathematical software MATLAB was also employed to average each of the 25 frequency responses for each cell into a single FRF for the cell. As discussed in Section 3, based on the

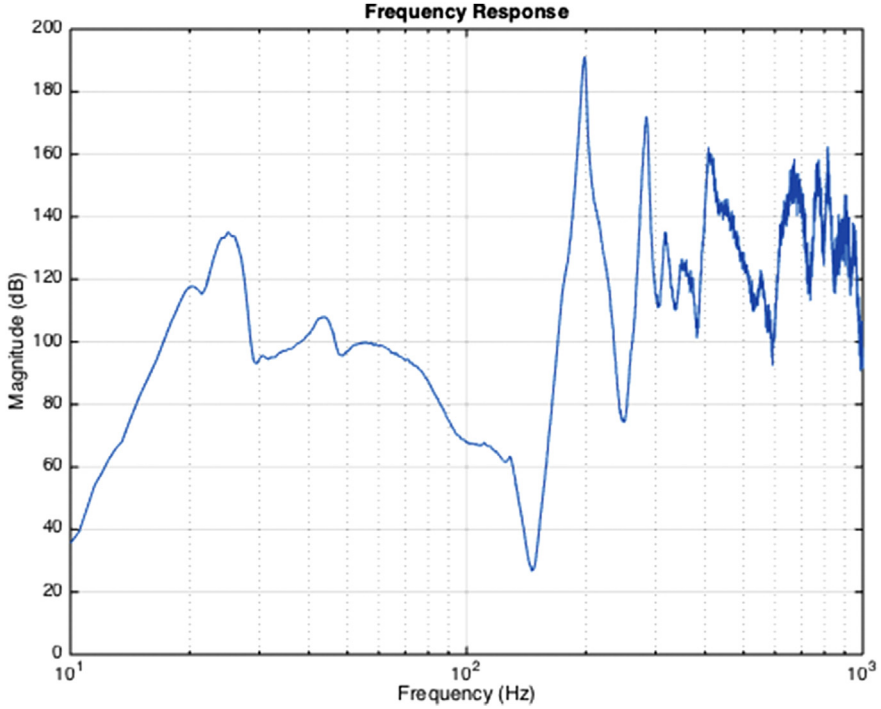

Fig. 4. Example frequency response showing the free–free test condition for the cells.

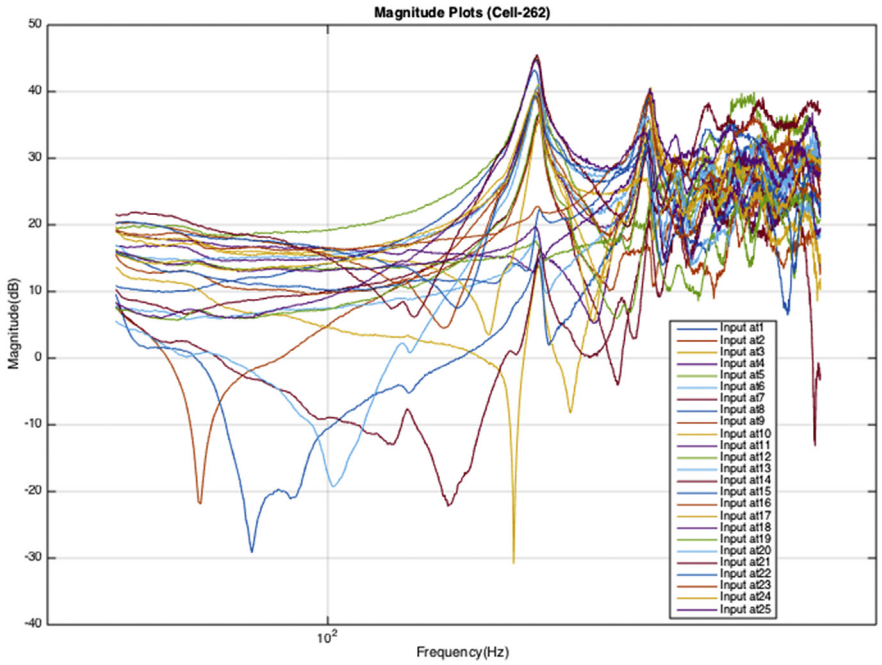

Fig. 5. Cell 262 – frequency response (magnitude plots) for each impact location.

average frequency response and through Equations (7)–(8), it is possible to estimate the damping for each natural frequency and the bulk stiffness of the cell.

5. Results

5.1. Cell natural frequencies and modal shapes

Fig. 5 presents the twenty-five frequency response (magnitude) plots for Cell 262 that correspond to each impact location defined in Fig. 3. Using MATLAB, an averaged FRF was calculated for the cell. Figs. 6 and 7 present the gain and phase components of the averaged FRF respectively. As it can be seen, the cell exhibits seven natural frequencies (represented by the peaks in the magnitude plot and a corresponding transition in the phase plot). The coherence plot presented in Fig. 8 demonstrates a high degree of correlation between the input and output energy levels (greater than 92%) for frequencies up to 400 Hz. Above this threshold the

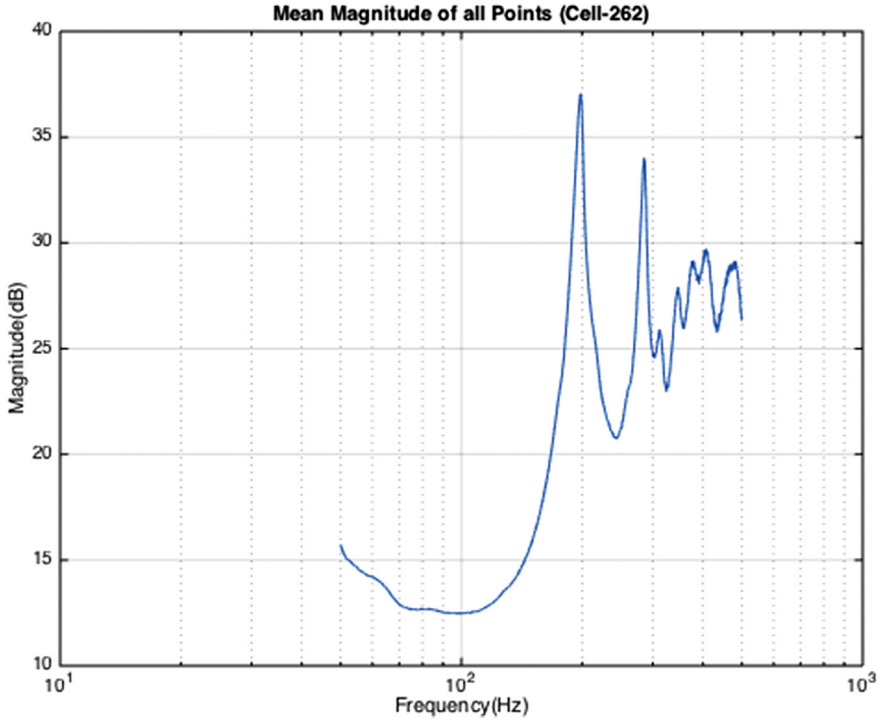

Fig. 6. Cell 262 – averaged frequency response (magnitude plot).

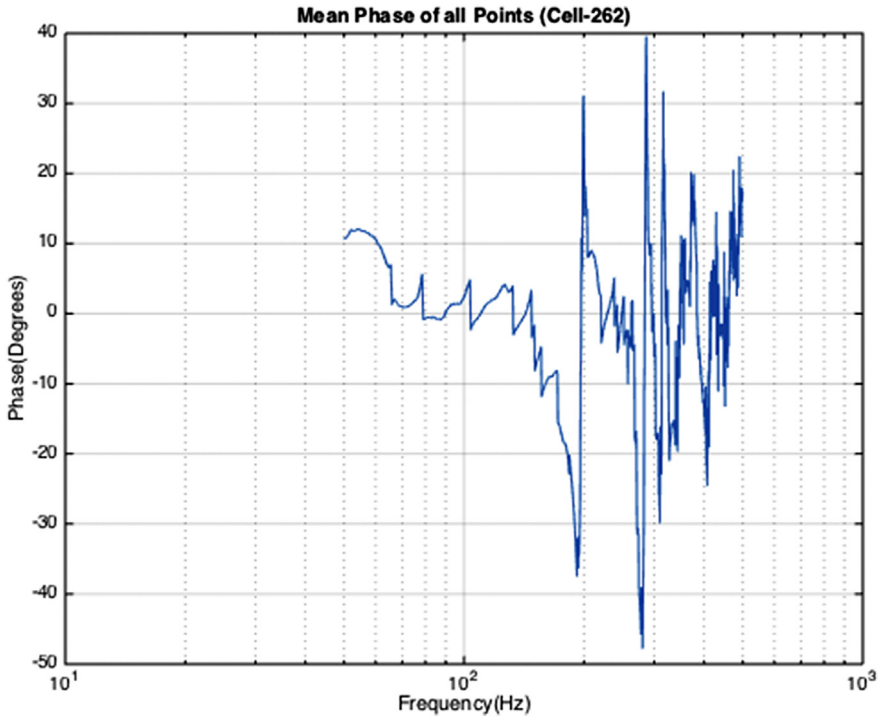

Fig. 7. Cell 262 – averaged frequency response (phase plot).

coherence value reduce as external disturbances and non-linearities dominate the cell's response. As discussed in Section 4.3, taking the geometry of the cell into consideration it is possible to identify the mode shapes for the cell. Fig. 9 presents the seven mode shapes calculated through the IDEAS software. Video 1, available within the electronic version of this paper, presents the animated version of Fig. 9 and clearly shows the interaction between the different torsional and bending modes excited within the cell.

Supplementary video related to this article can be found at http://dx.doi.org/10.1016/j.jpowsour.2015.03.098

Table 2 presents the complete results from the modal analysis. The table defines the natural frequencies measured for each cell. As it can be seen, irrespective of the SOC value, the same initial four

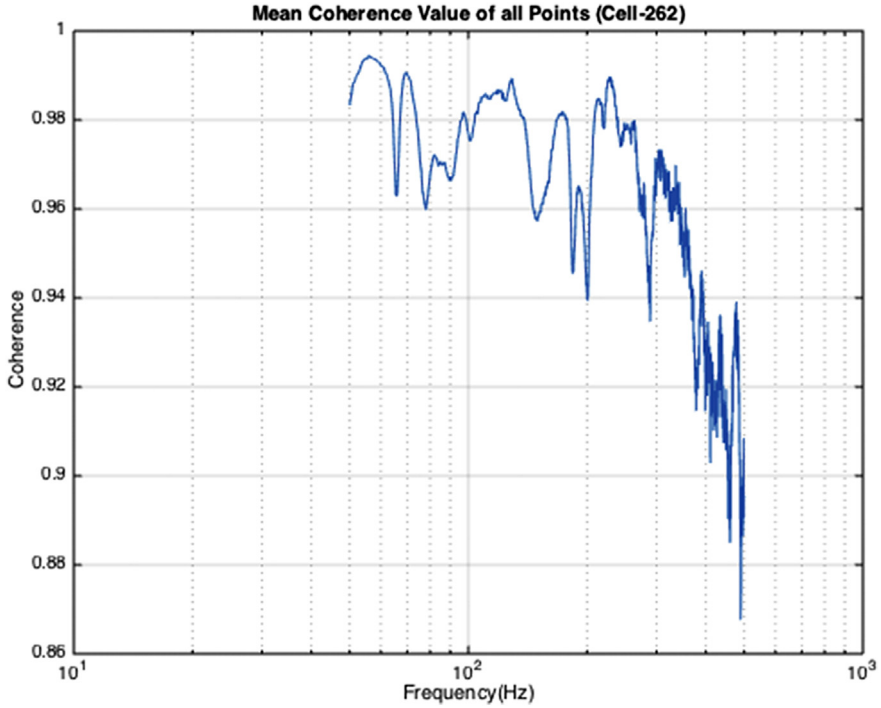

Fig. 8. Cell 262 – coherence plot.

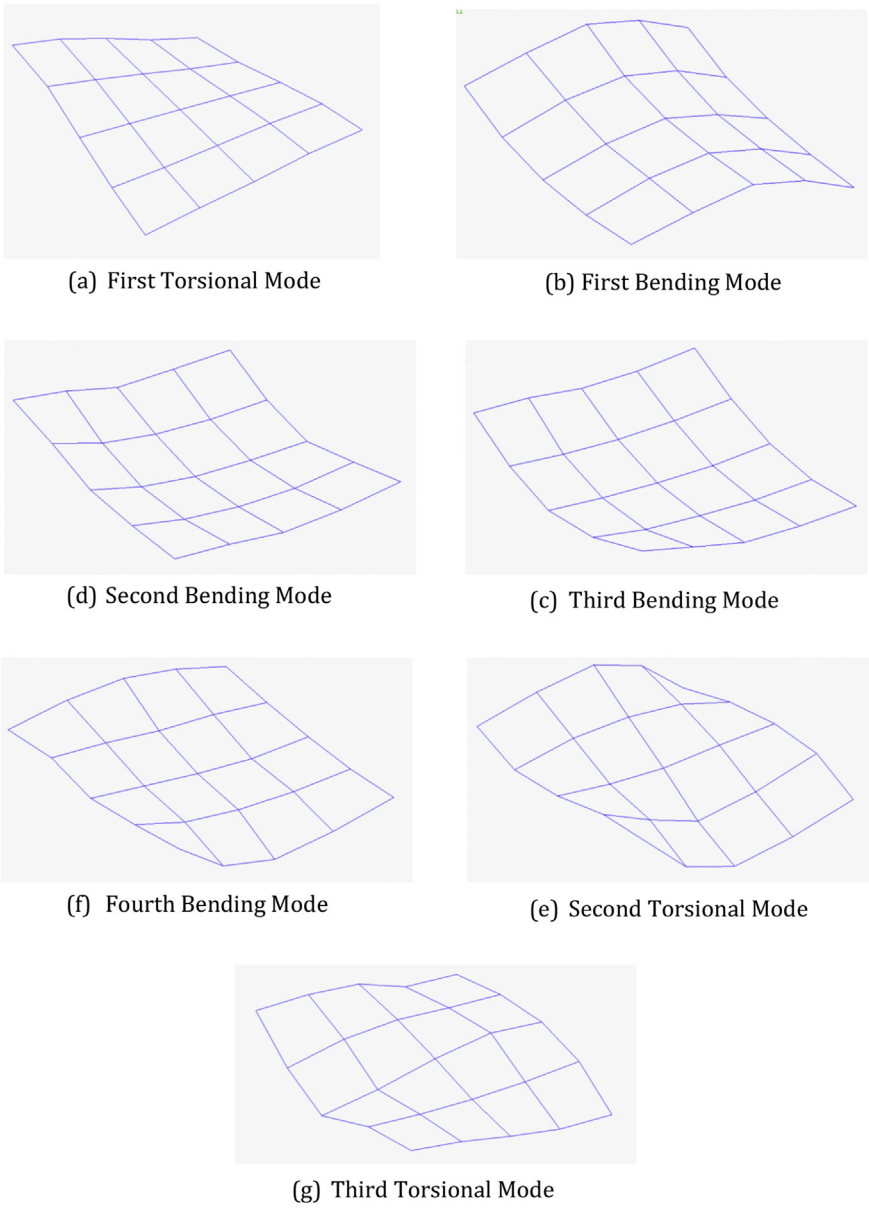

Fig. 9. Cell 262 – seven modal shapes corresponding to each natural frequency.

Table 2
Estimated natural frequencies for each cell corresponding to the seven mode shapes identified.

Cell ID	SOC (%)	First torsional mode (Hz)	First bending mode (Hz)	Second bending mode (Hz)	Third bending mode (Hz)	Fourth bending mode (Hz)	Second torsional mode (Hz)	Third torsional mode (Hz)
259	10	191.5	271.5	293	351		408	468
267	10	203.5	291	316	337.5	380	442	489.5
268	10	202	296	307	357		403.5	474
260	25	195	278.5	293.5	347	370	414	475
261	25	186	267.5	316	336			
266	25	193	289.5	334.5	360	378.5	401.5	453.5
262	50	197.5	285.5	313	346.5	377.5	407	478.5
264	50	200.5	286	313	367.5	389		446.5
265	50	197.5	262.5	288	339.5	380	410	461
263	75	201	283.5	298.5	357.5	386	412.5	471
269	75	199	282.5	297.5	340.5	378	395.5	456.5
270	75	201.5	294.5	323	342.5	389.5	423	472.5
273	90	200.5	282.5	305	353	397.5	417.5	491
275	90	205.5	287.5	306	356	396	416	478
276	90	204	285	306	343.5	389.5	434	480

Table 3
Calculated damping coefficient for each cell and natural frequency.

Cell ID	SOC (%)	First torsional mode (damping ratio)	First bending mode (damping ratio)	Second bending mode (damping ratio)	Third bending mode (damping ratio)	Fourth bending mode (damping ratio)	Second torsional mode (damping ratio)	Third torsional mode (damping ratio)
259	10	0.0196	0.0133	0.0198	0.0147		0.0109	0.0155
267	10	0.0052	0.0074	0.0204	0.0266	0.0151	0.0152	0.0096
268	10	0.0038	0.0119	0.0133	0.0191		0.0105	0.0053
260	25	0.0075	0.0132	0.0207	0.0129	0.0214	0.0205	0.0197
261	25	0.0160	0.0289	0.0249	0.0262			
266	25	0.0128	0.0096	0.0225	0.0162	0.0149	0.0136	0.0124
262	50	0.0071	0.0100	0.0256	0.0203	0.0174	0.0163	0.0176
264	50	0.0050	0.0093	0.0174	0.0231	0.0141		0.0084
265	50	0.0080	0.0321	0.0106	0.0202	0.0149	0.0182	0.0156
263	75	0.0067	0.0204	0.0139	0.0247	0.0168	0.0199	0.0158
269	75	0.0106	0.0140	0.0175	0.0225	0.0149	0.0189	0.0191
270	75	0.0063	0.0077	0.0217	0.0287	0.0112	0.0173	0.0142
273	90	0.0105	0.0102	0.0254	0.0075	0.0268	0.0118	0.0155
275	90	0.0080	0.0160	0.0121	0.0231	0.0130	0.0185	0.012
276	90	0.0058	0.0170	0.0114	0.0237	0.0131	0.0156	0.011

Table 4
Average damping coefficients for each SOC threshold.

SOC (%)	First torsional mode (average damping ratio)	First bending mode (average damping ratio)	Second bending mode (average damping ratio)	Third bending mode (average damping ratio)	Fourth bending mode (average damping ratio)	Second torsional mode (average damping ratio)	Third torsional mode (average damping ratio)
10	0.0095	0.0109	0.0178	0.0201	0.0151	0.0122	0.0101
25	0.0121	0.0172	0.0227	0.0184	0.0182	0.0171	0.0161
50	0.0067	0.0171	0.0179	0.0212	0.0155	0.0173	0.0139
75	0.0079	0.0140	0.0177	0.0253	0.0143	0.0187	0.0164
90	0.0081	0.0144	0.0163	0.0181	0.0176	0.0153	0.0128

Table 5
Linear regression equations for the damping coefficient (y) vs. SOC (x).

Mode	Linear regression equation
First Torsional Mode (Hz)	y = -4E-05x + 0.0107
First Bending Mode (Hz)	y = 1E-05x + 0.014
Second Bending Mode (Hz)	y = -4E-05x + 0.0206
Third Bending Mode (Hz)	y = 2E-05x + 0.0196
Fourth Bending Mode (Hz)	y = 1E-06x + 0.0161
Second Torsional Mode (Hz)	y = 4E-05x + 0.0142
Third Torsional Mode (Hz)	y = 3E-05x + 0.0125

Table 6
Calculated cell stiffness.

Cell ID	SOC (%)	Cell weight (g)	Stiffness constant (Nm^{-1})
259	10	577	835358.90
267	10	577	866173.26
268	10	577	789429.70
260	25	577	890065.11
261	25	578	921891.24
266	25	576	917310.42
262	50	578	886985.30
264	50	578	847026.19
265	50	576	943331.59
263	75	578	929476.23
269	75	577	902073.04
270	75	578	926483.47
273	90	573	909375.21
275	90	576	960297.66
276	90	575	944686.95

modes (torsion, bending, bending and bending) are present in each cell at frequencies in the order of: 191–205 Hz; 262–296 Hz; 288–334 Hz and 337–360 Hz respectively. However, above approximately 350 Hz some of the cells exhibit different dynamic behavior. For example, the fourth bending mode is only present in a subset of the cells charged to 10% and 25% SOC. Similarly, from the frequency response data measured for Cell 264 there was no discernable resonance at: 400 Hz (corresponding to the second torsional mode) and for cell 261, it was not possible to identify any resonances above 336 Hz. One reason for this can be seen from the corresponding coherence plot for cell 261 that clearly shows a reduction in coherence to nearly 40%. The most likely reason for this is operator error during the experiment.

Table 7
Averaged cell stiffness for each SOC threshold.

SOC (%)	Mean stiffness at cell weight (Nm^{-1})
10	830320.62
25	909755.59
50	892447.69
75	919344.25
90	938119.94

Acknowledging the sample size for this experiment is relatively small; the results presented in Table 2 imply that the natural frequencies for the Li-ion cell are not dependent on the cells SOC. Differences in resonance, between cells, for a given SOC are most likely attributable to cell-to-cell variations resulting from the manufacturing processes employed. As part of the study, the mass and dimensions (width, length and thickness) of each cell were recorded and differences in the order of 1 mm were noted between the thinnest and thickest cell. It is noteworthy that 80% of cells tested were outside of the specified manufacturing tolerance for thickness, at one or more measurement location.

5.2. Cell damping

Table 3 presents the damping coefficient (ς) calculated from Equation (8) for each of the seven mode shapes and for each cell.

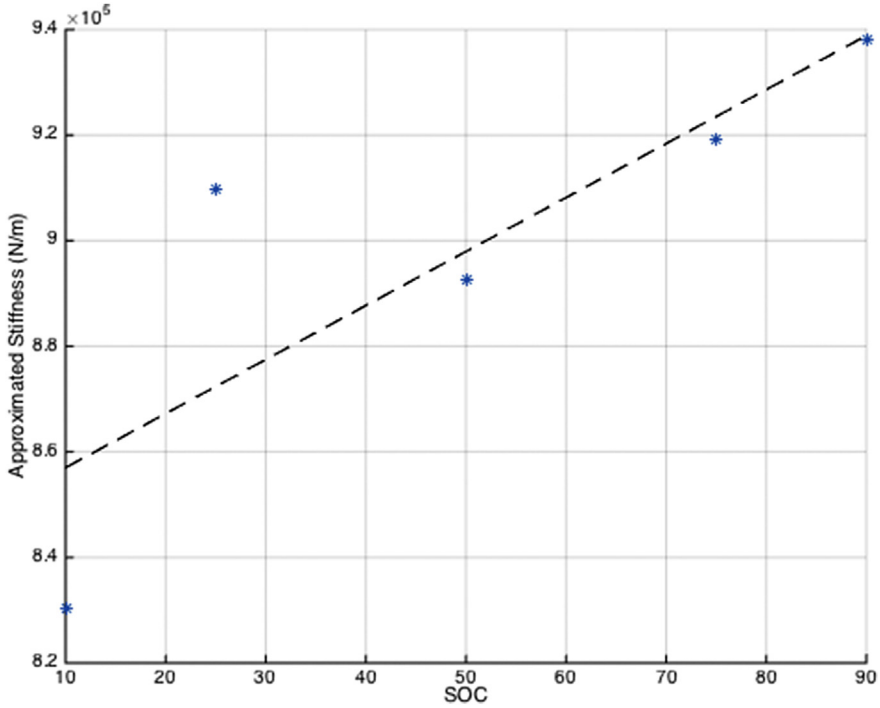

Fig. 10. Average cell stiffness vs. cell SOC.

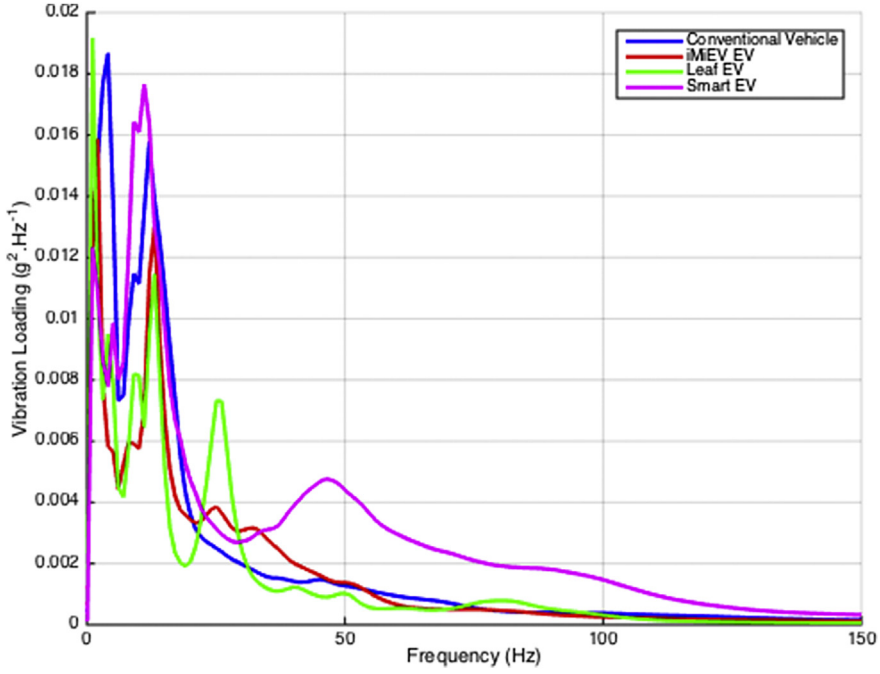

Fig. 11. PSD Plot (X, Y, Z – axis) vibration of a Nissan Leaf battery subject to durability surfaces.

Table 4 presents the averaged values of ς for each SOC threshold. MATLAB was further employed to generate a linear best-fit function defining the relationship between cell damping and SOC. The results are presented in Table 5 and highlight that, given the sample-size and cell technology tested, there does not appear to be a discernable relationship between the damping for each natural frequency and cell's SOC.

5.3. Cell stiffness

Table 6 presents the calculated stiffness (k_c) for each cell based on the 1st natural frequency (measured between 191 and 205 Hz). Equation (7) was employed to calculate k_c. For completeness, the measured value of cell mass (m_c) was used in the calculations and is provided for reference. As discussed in Section 5.1, variations in cell

mass were found to be in the order of 1 mm. Table 7 presents the mean stiffness value corresponding to each SOC threshold. Fig. 10 presents a graphical representation of Table 7 and clearly indicates a trend of increasing k_c for higher values of SOC. This result contradicts that observed in Section 5.1 that shows insensitivity between the cells natural frequency and SOC. For a simple mechanical structure, in accordance with Equation (7), one would expect to see an increase in natural frequency as the stiffness of the specimen is increased (with mass held constant). At present, only the experimental data and observations are noted. Additional experiments and further modeling activity is ongoing within the University. The aim of these additional tests is to reaffirm the results presented here and, if appropriate, to formulate a rationale for the observed behavior.

5.4. Implications for in-vehicle performance

The results presented highlight that the first natural frequency of the cells tested (irrespective of SOC) occurs at a frequency in excess of 180 Hz. A study presented in Ref. [19] that measured the vibration inputs to a series of commercially available EV battery installations found that the majority of road-induced vibration occurs within the frequency range of 0–150 Hz. This is illustrated in Fig. 11 that highlights the vibration energy measured in the z-axis within the Nissan Leaf, the Smart EV and the Mitsubishi i-MiEV that has been sequenced to a 100,000 miles of vehicle durability. Further information regarding the derivation of Fig. 11 is available within [19] and will therefore not be repeated here. Comparing the isolated cell data from Section 5 with the in-vehicle data published in Refs. [19,20] indicates that it is unlikely that these NMC pouch cells would be excited by road surface vibration. However, it is noteworthy that Fig. 11 corresponds to the vibration energy measured on the surface of the battery pack and this may differ to that experienced within the battery enclosure. Additional higher frequency vibrations may be induced from the thermal management systems, the power electronics and the use of cell-level restraints [19]. Further research to quantify the in-vehicle, cell-level vibration loading is the subject of on-going research within the University.

6. Further work

To reaffirm the results presented here it is necessary to do further tests. These tests will evaluate the same cell for different SOC values. This would highlight any possible relationship between SOC and natural frequency without the impact of cell-to-cell variations introducing uncertainty to the results obtained. While this initial study focused on the SOC range of 10%–90%, a further study will characterize the cell at the extremes of operation that will be experienced within an EV, namely less than 10% SOC and greater then 90% SOC. Introducing temperature as another variable to the experimental set-up that could yield interesting results for the vehicle manufacturer or battery systems integrator. While this study has concluded that there is little evidence to suggest that SOC impacts the frequency response of an NMC 25 Ah laminate pouch cell, further investigation is required to identify if these results are transferable to other cell chemistries and form-factors currently being investigated by the automotive industry. As discussed in Section 5.4, a further investigation should determine the cell-level vibration induced loading from the complete battery enclosure when excited from a road induced vibration and other ancillaries within the EV or HEV. For such a study, a *grounded* (rather than a free–free) test method may be more appropriate since this will allow the evaluation of the cell within the correct orientation and restraint for the battery pack design under investigation.

7. Conclusions

The authors argue that if future EV and HEV battery systems are to be designed such that the impact of vibration induced resonance is minimized, engineers must have a rigorous understanding of key system attributes such as the natural frequencies of the cell, the level of damping present and the mode shapes induced under mechanical load. This paper has presented the underpinning theory and experimental method employed to ascertain the FRF and mode shapes for a range of commercially available 25 Ah NMC Laminate Pouch Cells. Each cell was pre-conditioned to a different value of SOC. The primary conclusions that can be drawn from the results presented are firstly, irrespective of cell SOC, the same initial four modes (torsion, bending, bending and bending) are present in each cell and occur within a frequency range of 191 Hz–360 Hz. Further, the results imply that the natural frequencies are not dependent on the cell's SOC and are most likely attributable to subtle cell-to-cell variations resulting from the manufacturing processes employed. Secondly, the approximated damping calculated for each natural frequency within each cell suggests that there is no discernable relationship between the value of damping present and cell's SOC. Finally, the lowest natural frequency recorded within the cells is above the frequency range (0–150 Hz) typically associated with road-induced vibration. As a result, it is unlikely that these NMC pouch cells will be excited by road surface vibration.

Acknowledgments

The research presented within this paper is supported by the Engineering and Physical Science Research Council (EPSRC - EP/I01585X/1) through the Engineering Doctoral Centre in High Value, Low Environmental Impact Manufacturing. The research was undertaken in collaboration with the WMG Centre High Value Manufacturing Catapult (part-funded by Innovate UK) in collaboration with Jaguar Land Rover and TATA Motors. The authors would like to express their gratitude to Sound and Vibration Technology Ltd for their support and advice throughout the test program.

References

[1] S.-I. Moon, I.-J. Cho, D. Yoon, J. Mech. Sci. Technol. 25 (2011) 611–637.
[2] H.Y. Choi, J.S. Lee, Y.M. Kim, H. Kim, in, Hongik University, Seoul, South Korea, 2013, pp. 1–10.
[3] P. Dallard, A.J. Fitzpatrick, A. Flint, S.L. Bourva, A. Low, R.M.R. Smith, M. Willford, Struct. Eng. 79 (2001) 17–33.
[4] I. Avdeev, M. Gilaki, J. Power Sources 271 (2014) 382–391.
[5] X. Zhang, T. Wierzbicki, J. Power Sources 280 (2015) 47–56.
[6] L. Berla, S. Woo Lee, Y. Cui, W. Nix, J. Power Sources 273 (2015) 41–51.
[7] L. Greve, C. Fehrenbach, J. Power Sources 214 (2012) 377–385.
[8] K.-Y. Oh, J. Siegel, L. Secondo, S.U. Kim, N. Samad, J. Qin, D. Anderson, K. Garikipati, A. Knobloch, B. Epureanu, C. Monroe, A. Stefanopoulou, J. Power Sources 267 (2014) 197–202.
[9] E. Sahraei, J. Meiera, T. Wierzbicki, J. Power Sources 247 (2014) 503–516.
[10] X. Feng, J. Sun, M. Ouyang, F. Wang, X. He, L. Lu, H. Peng, J. Power Sources 275 (2015) 261–273.
[11] X. Liu, S. Stoliarov, M. Denlinger, A. Masias, K. Snyder, J. Power Sources 280 (2015) 516–525.
[12] N. Spinner, C. Field, M. Hammond, B. Williams, K. Myers, A. Lubrano, S. Rose-Pehrsson, S. Tuttle, J. Power Sources 279 (2015) 713–721.
[13] U. Nations, in, United Nations, 2002.
[14] ECE, Economic and Social Council ECE/TRANS/WP.29/2012/102, 2013, pp. 1–54.
[15] L. Florence, in, Underwriters Laboratory Inc., 2013, pp. 1–19.
[16] U. Nations, in, United Nations, New York, 2011, pp. 62.
[17] U. Nations, in: 38.3 Lithium Metal and Lithium Ion Batteries, United Nations, 2008, pp. 43–51.
[18] K. Kleiner, D. Dixon, P. Jakes, J. Melke, M. Yavuz, C. Roth, K. Nikolowski, V. Liebau, H. Ehrenberg, J. Power Sources 273 (2015) 41–51.
[19] J. Hooper, J. Marco, J. power sources 245 (2014) 510–519.
[20] J. Hooper, J. Marco, in: HEVC 2013-4th Hybrid and Electric Vehicles Conference, IET, England, London, 2013, pp. 1–6.
[21] Y. Choi, D. Jung, K. Ham, S. Bae, Procedia Eng. 10 (2011) 851–856.

[22] A. Bilošová, in: Investments in Education Development, 2011, pp. 1–120.
[23] B. Schwartz, M. Richardson, CSI Reliability Week, 1999, pp. 1–12.
[24] T. Harrison, in: Brüel & Kjær Sound & Vibration Measurement, 2003, pp. 1–84. Royston, Hertfordshire.
[25] P. Avitabile, Sound and Vibration, 2001, pp. 3–11.
[26] R. Bono, in: IMAC XXVI: Conference & Exposition on Structural Dynamics – Technologies for Civil Structures, The Modal Shop,, 2011.
[27] https://www.endevco.com/download/TP312.pdf, in, Endevco, 2014, pp. 1–7.
[28] http://zone.ni.com/reference/en-XX/help/372416F-01/svtconcepts/svfreqresponse/, in, National Instruments Corporation, 2014.
[29] http://zone.ni.com/reference/en-XX/help/372416A-01/svtconcepts/use_freq_ana_vis/, in, National Instruments Corporation, 2009.
[30] P. Avitabile, in: University of Massachusetts, University of Massachusetts Lowell, pp. 1–12.